# **Geophysical Research Letters**

#### **RESEARCH LETTER**

10.1029/2020GL087181

### **Key Points:**

- We present a novel backprojection approach to image time-lapse coseismic rupture propagation for the 2019 Ridgecrest earthquake sequence
- The backprojection images agree with the fault geometry determined by the distribution of aftershocks
- The time-lapse images illustrate the detailed rupture processes of the M<sub>w</sub>6.4 foreshock and M<sub>w</sub>7.1 mainshock

#### **Supporting Information:**

- · Supporting Information S1
- · Text S1

#### Correspondence to:

J. Yang, Jidong.Yang@utdallas.edu

#### Citation

Yang J., Zhu, H., & Lumley, D. (2020). Time-lapse imaging of coseismic ruptures for the 2019 Ridgecrest earthquakes using multiazimuth backprojection with regional seismic data and a 3-D crustal velocity model. *Geophysical Research Letters*, 47, e2020GL087181. https://doi.org/10.1029/2020GL087181

Received 22 JAN 2020 Accepted 15 APR 2020 Accepted article online 23 APR 2020 Time-Lapse Imaging of Coseismic Ruptures for the 2019 Ridgecrest Earthquakes Using Multiazimuth Backprojection With Regional Seismic Data and a 3-D Crustal Velocity Model

Jidong Yang<sup>1</sup>, Hejun Zhu<sup>1</sup>, and David Lumley<sup>1</sup>

<sup>1</sup>Department of Geosciences, Department of Physics, The University of Texas at Dallas, Richardson, TX, US

**Abstract** Using regional seismic data and a 3-D crustal velocity model, we develop a novel multiazimuth backprojection approach and apply it to image time-lapse coseismic ruptures for the 2019 Ridgecrest earthquakes. The time-integrated images for the  $M_{\rm w}$ 6.4 foreshock and  $M_{\rm w}$ 7.1 mainshock agree with the fault geometry delineated by the aftershock distributions. Backprojection images at different times illustrate the detailed rupture processes for these two events. For instance, the  $M_{\rm w}$ 6.4 foreshock initialized close to the hypocenter, then the rupture propagated along a northwest trending fault with an average velocity of 1.0 km/s, and finally jumped to a southwest trending fault and propagated about 20 km with a velocity about 1.5 km/s. In contrast, the  $M_{\rm w}$ 7.1 mainshock initialized near the hypocenter, then propagated to the northwest upon reaching the Coso volcanic field with an average velocity of 1.4 km/s, and later turned to the southeast and propagated along the main fault zone with a complex bilateral process and a velocity about 0.6 km/s.

# 1. Introduction

In July 2019, a sequence of damaging earthquakes occurred close to the city of Ridgecrest, California. It started on 4 July with an  $M_w$ 6.4 foreshock, followed by an  $M_w$ 7.1 mainshock 34 hr later (Brandenberg et al., 2019). It was the largest event in the Eastern California Shear Zone since the Hector Mine earthquake ( $M_w$ 7.1) occurred on 16 October 1999. By analyzing geodetic, seismic and seismicity data, Ross et al. (2019) showed that the Ridgecrest sequence ruptured on an unmapped multiscale network of interlaced orthogonal faults, and the complex fault geometry persists over the entire seismogenic depth. Barnhart et al. (2019) used interferometric synthetic aperture radar to characterize surface displacements and constrain subsurface slips. Their analysis for the static stress change suggested that the foreshock sequence systematically promoted slips at the hypocenter of the  $M_w$ 7.1 mainshock. Furthermore, Liu et al. (2019) presented kinematic finite-fault models for these two events using seismological and geodetic data, which showed slow rupture velocities (1.0–1.5 km/s) for this immature fault system. Using remote sensing observations, high-rate GPS data and seismological waveforms, (Chen et al., 2020) proposed detailed source models for these two earthquakes, which show complex cascading and pulse-like rupture processes.

Identifying and characterizing earthquakes are important to estimate potential disasters and guide a rapid rescue response (Allen & Kanamori, 2003; Hayes, 2011; Satriano et al., 2008). Determining source parameters, including hypocenter location, fault geometry, slip distribution, and rupture processes, is one of the major aspects for earthquake characterization. Using local, regional, and teleseismic data, the hypocenter and source mechanism can be estimated by fitting observed and predicted waveforms (Dziewonski et al., 1981; Dziewonski & Woodhouse, 1983; Hayes et al., 2009; Liu et al., 2004). Through inverting high-rate displacement records from GPS, the moment magnitude, fault geometry, and slip distribution can be evaluated in near real time (Crowell et al., 2009, 2012; Falck et al., 2010; Johnson et al., 2001; Johnson & Segall, 2004; Melgar et al., 2012; Minson et al., 2014; Yue et al., 2014).

For small-to-intermediate events, earthquakes can be approximated as point sources, and their moment tensor solutions can be used to describe magnitude, fault plane geometry and faulting mechanism. For large events (e.g.,  $M_w \ge 6$ ), the point source model is insufficient to explain the long duration, directivity, and waveform spectra of ground motions (Atkinson, 1993; Atkinson & Silva, 1997; Beresnev & Atkinson, 2002).

©2020. American Geophysical Union. All Rights Reserved.

YANG ET AL. 1 of 11

In contrast, the finite-fault model, introduced by Hartzell (1978), is capable of describing the ground motion characteristics of large earthquakes and has been popular for studying local slip, rake angle, rise time, and rupture velocity of complex faulting processes (Atzori et al., 2009; Dettmer et al., 2014; Ji et al., 2001, 2002; Liu & Archuleta, 2004; Tinti et al., 2016; Wald & Heaton, 1994). In finite-fault modeling and inversion, the fault geometry is typically used as a priori information. Therefore, the accuracy of estimated subfault parameters depends on a priori knowledge about the fault geometry. Using the concept of time-reversal imaging, Ishii et al. (2005) proposed backprojection analysis for locating earthquake sources and examining complex rupture propagations. This approach requires minimal a priori constraint and can be implemented by assigning summed data to each grid point according to the traveltimes of different seismic phases (Kiser & Ishii, 2017). The simplicity and robustness of backprojection analysis make it popular in many earthquake studies (D'Amico et al., 2010; Kiser et al., 2011; Koper et al., 2012; Meng et al., 2016; Walker & Shearer, 2009; Wang & Mori, 2011; Xu et al., 2009). The time shifts used in backprojection are commonly calculated by summing ray theoretical traveltimes calculated from a given 1-D velocity model with empirical corrections (Kiser & Ishii, 2017). This makes it difficult to accurately account for the complicated physics of wave propagation in a 3-D heterogeneous Earth. Recently, Liu et al. (2017) utilized traveltimes calculated from a 3-D global P wave tomography model in backprojection and obtained higher spatial resolution for backprojection results than those derived from 1-D velocity models.

Previous backprojection studies have been commonly applied to teleseismic data from one or a few dense receiver arrays. Taking advantage of the well-sampled dense spatial coverage of local seismic networks deployed in Southern California, we develop a novel multiazimuth backprojection approach and apply it to the 2019 Ridgecrest earthquake sequence to image its time-lapse coseismic rupture processes. The geometric mean imaging condition (Nakata & Beroza, 2016) is incorporated into backprojection to suppress illumination artifacts caused by uneven station distributions and to improve spatial resolution. A 3-D crustal velocity model developed by Lin et al. (2010) for Southern California and a fast marching solver (Fomel, 1997) are used to compute first-arrival traveltimes, which automatically accounts for lateral velocity heterogeneities within the crust, and does not require any empirical traveltime calibrations as used in classical teleseismic backprojection. The stacked backprojection images for the  $M_{w}$ 6.4 and  $M_{w}$ 7.1 events agree with the fault geometry determined by the aftershocks from the South California Earthquake Data Center (SCEDC) catalog. The time-lapse images illustrate the detailed rupture processes of the  $M_w$ 6.4 foreshock and  $M_w$ 7.1 mainshock. For instance, the  $M_w$ 6.4 foreshock initialized close to the hypocenter, then ruptured along a northwest trending fault, and finally propagated to the southwest. The  $M_w$ 7.1 mainshock initialized near its hypocenter, then first propagated to the northwest until arriving at the Coso volcanic region, and later turned to the southeast and propagated along the main fault zone with a complex bilateral faulting process.

## 2. Multiazimuth Backprojection Using Local Seismic Networks

For seismograms  $u(\mathbf{x}_r,t)$  recorded by dense local seismic networks, we first cluster them into different azimuths with respect to the epicenter. Then, the geometric mean imaging condition is incorporated into the backprojection for each set of azimuth-clustered seismograms (Nakata & Beroza, 2016), which can be expressed as

$$I(\mathbf{x},t) = \prod_{i_{nr}=1}^{N_{az}} \int_{t-\Delta t}^{t+\Delta t} \left[ \sum_{\mathbf{x}_r} u_{i_{az}} \left( \mathbf{x}_r, t' + \tau(\mathbf{x}_r, \mathbf{x}) \right) \right]^2 dt'$$
 (1)

where  $\mathbf{x}$  denotes the potential earthquake source location and  $\mathbf{x}_r$  is the seismic receiver location. The  $\tau(\mathbf{x}_r, \mathbf{x})$  is the traveltime from the station  $\mathbf{x}_r$  to the potential source location  $\mathbf{x}$ . The  $u_{i_{az}}(\mathbf{x}_r, t')$  is the seismogram clustered in the  $i_{az}$ th azimuth, and  $N_{az}$  is the total number of azimuth clusters. The t' is the time integration variable, with limits determined by t as the propagation time relative to the P wave traveltime at the hypocenter location, and  $\Delta t$  is the half time window for computing the energy to form the time-lapse image  $I(\mathbf{x},t)$ .

The differences between the multiazimuth backprojection in equation (1) with classical teleseismic backprojection (Ishii et al., 2005; Kiser & Ishii, 2017) include the following aspects. First, we use a fast marching solver and a 3D crustal velocity model to compute the traveltime  $\tau(\mathbf{x}_r, \mathbf{x})$  by solving the Eikonal equation, which is more accurate than ray-tracing approaches and more computationally efficient than wave-equation methods. This allows us to automatically consider lateral velocity heterogeneities within the crust, and

YANG ET AL. 2 of 11

therefore it does not require any empirical traveltime calibrations. Second, the geometric mean imaging condition is used to compute the backprojection images by multiplying instead of summing results with different azimuths. As analyzed by Nakata and Beroza (2016), the geometric mean imaging condition allows us to suppress artifacts caused by uneven station coverages with different offsets and azimuths and produce high-resolution images at true source locations. Third, seismograms recorded by local networks instead of teleseismic waveforms are used in this multiazimuth backprojection, which have short propagation distances and therefore need careful data processing to separate primary P waves from following S waves, surface waves, coda and other reverberations due to local velocity heterogeneities within the crust. On the other hand, these local network waveforms enable us to better constrain coseismic rupture processes and avoid imaging contaminations and artifacts from the propagation of seismic waves along long traveling paths within the crust and mantle. In addition, regional waveforms are backprojected onto a 3-D volume, and thus this method does not need a priori constraint for the fault geometry.

# 3. Data Processing and the 3-D Crustal Velocity Model

Seismograms for the 2019 Ridgecrest  $M_{\rm w}6.4$  and  $M_{\rm w}7.1$  events are collected from the SCEDC (https://scedc.caltech.edu/). Since the observed horizontal components have weak P waves and much weaker signal-to-noise ratio than vertical components, only vertical components are used for regional multiazimuth backprojection analysis in this study. Within the study area (Figure 1a), there are 494 and 517 stations with recorded waveforms for the  $M_{\rm w}6.4$  foreshock and  $M_{\rm w}7.1$  mainshock, respectively. In the data processing step (Figure 1c), we first manually check the data quality and remove traces with signal-to-noise ratio less than 2. Then, we deconvolve the instrument responses to obtain displacement records. Next, we remove direct current frequency and linear trends, mute waveforms after primary S wave arrival times, apply a band-pass filter, and normalize traces with their maximum absolute values. The frequency band we used in this study is 0.2–5 Hz. Because the muted seismograms with different epicentral distances have different P wave traveltimes and durations, we remove the traces with P wave traveltimes less than 5 s and P wave durations less than 10 s to avoid strong nonlinear near-source effects and unbalanced summation in the backprojection analysis. The processed waveforms for the  $M_{\rm w}6.4$  foreshock and  $M_{\rm w}7.1$  mainshock are presented in Figures 1d and 1e.

With the 3-D crustal P wave velocity model developed by Lin et al. (2010), we utilize the fast marching method to solve the Eikonal equation (Fomel, 1997) and compute traveltimes from stations to potential source locations (Figures 1b and S1–S5 in the supporting information). The velocity model is discretized into a grid of  $49 \times 993 \times 905$  with a spatial mesh sampling of 0.5 km. The backprojection imaging domain is restricted to an area of  $100 \text{ km} \times 100 \text{ km}$  around the hypocenter, with the depth ranging from 0 to 20 km. Ten and fifteen azimuth clusters are used to image the foreshock and mainshock, respectively. The moving integration window  $(2\Delta t)$  is selected to be 3 s.

# 4. Coseismic Rupture Processes of the $M_w$ 6.4 Foreshock and $M_w$ 7.1 Mainshock

The time-integrated backprojection results using regional P waves are presented in Figure 2. The amplitudes of the backprojection images are normalized by their maximum values. The durations of the major energy release for the  $M_w$ 6.4 and  $M_w$ 7.1 events are about 12 and 20 s (Figures 2a and 2b), respectively. The accumulated radiation energy (Figures 2c) for the  $M_w$ 6.4 foreshock displays an "L-shape" pattern, which has a NE-SW segment and a NW-SE segment with the intersection around the epicenter. This geometry spatially correlates with the fault planes determined by the distribution of aftershocks from the SCEDC (purple dots in Figures 2c), which occurred during the 34 hr after the  $M_{\rm w}$ 6.4 foreshock (https://service.scedc.caltech. edu/eq-catalogs/date&urluscore;mag&urluscore;loc.php). The local maxima in the backprojection image are located at about 2 km north to the epicenter along the NW-SE segment, and about 10 km southwest of the epicenter along the NE-SW segment, respectively (Figures 2c and S6), indicating large slips occurred within these regions. In contrast, the accumulated backprojection image for the  $M_{\rm m}7.1$  mainshock shows a dominant NW-SE trending pattern, with an extension length around 50 km (Figures 2d). The large-amplitude region on the image (red and black colors in Figure 2d) agrees with the fault zone resolved by the aftershocks of four days after the  $M_w$ 7.1 mainshock (purple dots in Figures 2d). The maximum energy is located around the intersection of the main and cross faults, and this segment is wider than the northwest segment. One explanation is that the  $M_w$ 7.1 mainshock ruptured bilaterally and produced large radiation energy close to

YANG ET AL. 3 of 11

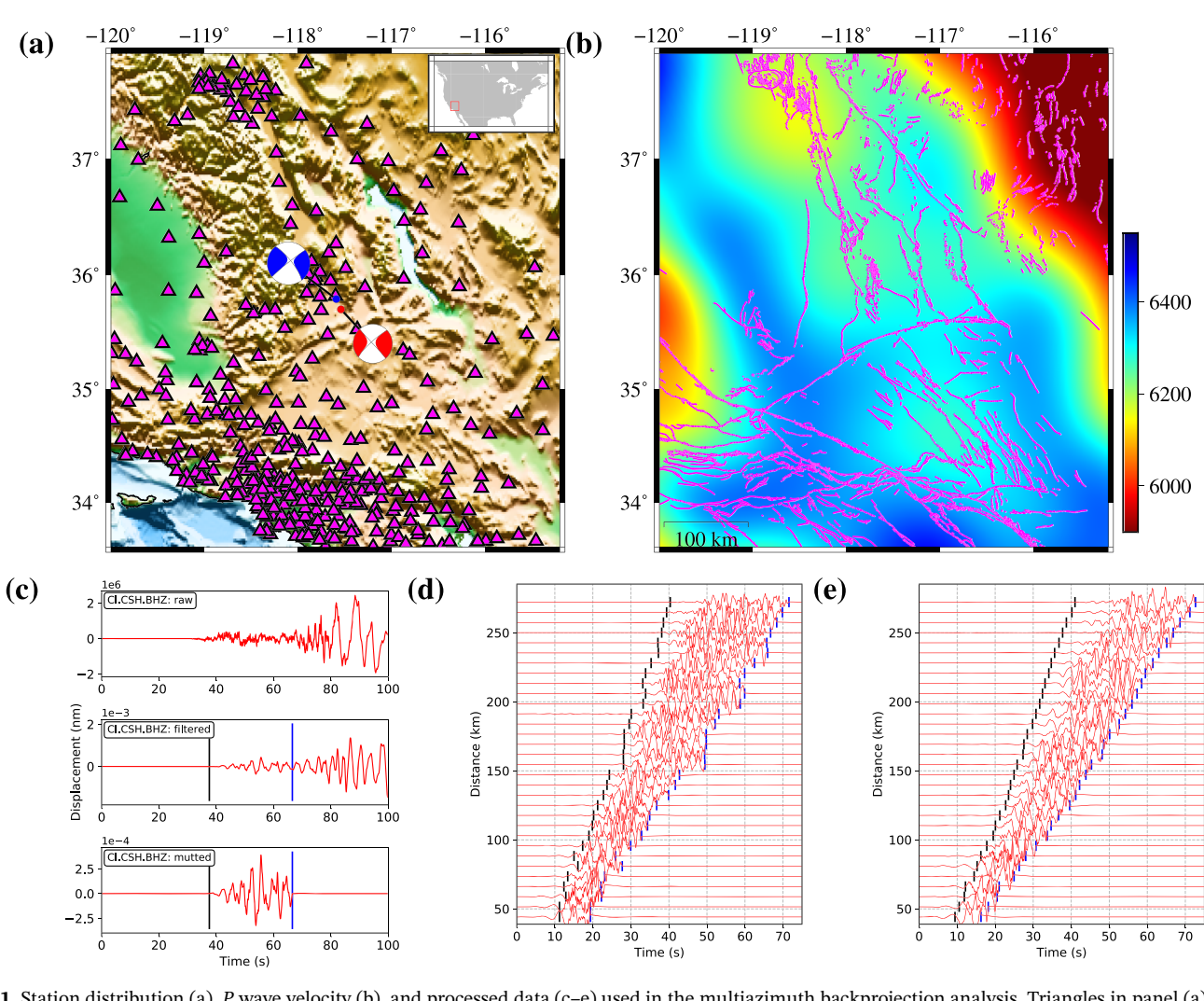


**Figure 1.** Station distribution (a), P wave velocity (b), and processed data (c-e) used in the multiazimuth backprojection analysis. Triangles in panel (a) denote stations used in this study, and red and blue beach balls represent the centroid moment tensor (CMT) solutions for the  $M_w$ 6.4 foreshock and  $M_w$ 7.1 mainshock, respectively. Panel (b) shows the map view of the 3-D P wave velocity model (Lin et al., 2010) at the depth of 5 km. Magenta lines denote the mapped Quaternary faults from USGS. Panel (c) illustrates data processing steps for the CI.CSH station, from top to bottom are raw, filtered and muted seismograms. Panels (d) and (e) are processed seismograms for the  $M_w$ 6.4 foreshock and  $M_w$ 7.1 mainshock, respectively. Black and blue vertical bars in panels (c)–(e) are P and S wave traveltimes computed using the 3-D crustal velocity models (Lin et al., 2010) and a fast marching solver (Fomel, 1997), respectively.

the intersection. In addition, the aftershock distribution from Ross et al. (2019) revealed many small-scale orthogonal faults near the main intersection. This complex fault geometry might produce resonances to amplify seismic wave amplitudes in the fault zone.

Because the wavefront curvatures along the depth direction are smaller than those on the map view, the depth resolution of the backprojection images is not as good as the horizontal resolution (Figures 2e–2h and S6). The radiation energy along the vertical profiles is smeared and even shows large amplitudes at depths greater than the seismogenic zone (Ross et al., 2019). However, the amplitude variations on the vertical profiles (Figures 2e and 2f) for the  $M_{\rm w}6.4$  foreshock indicate that large slips occur around the epicenter location, the maximum slip along the NE-SW fault segment is greater than that along the NW-SE fault segment, and the slips at the southwest end are mainly distributed at shallow depths. The spatial pattern of the large image amplitudes agrees with the slip distributions from Liu et al. (2019) and Ross et al. (2019). In contrast, the vertical profile for the  $M_{\rm w}7.1$  mainshock along the strike direction (Figure 2g) suggests that the depth of large slips gradually decreases from the southeast to the northwest, and the largest slip occurs about 10 km to the southeast of the epicenter. This slip distribution (Figure S9) is consistent with the finite-fault inversion result from Liu et al. (2019). It is notable that the vertical profile (Figure 2h), which is perpendicular to the main NW-SE strike direction, shows a radiation energy image with a nearly 90° dip, which supports

YANG ET AL. 4 of 11

1944807, 2020, 9, Downloaded from https://agupubs.onlinibiaray.iwiey.com/doi/0.1029/2020GL087181 by University Of Teasa - Dalats, Wiley Online Library on [16/02/2023]. See the Terms and Conditions (https://onlinelibiary.wiley.com/terms-and-conditions) on Wiley Online Library for rules of use, CA articles are governed by the applicable Created and the conditions of the c

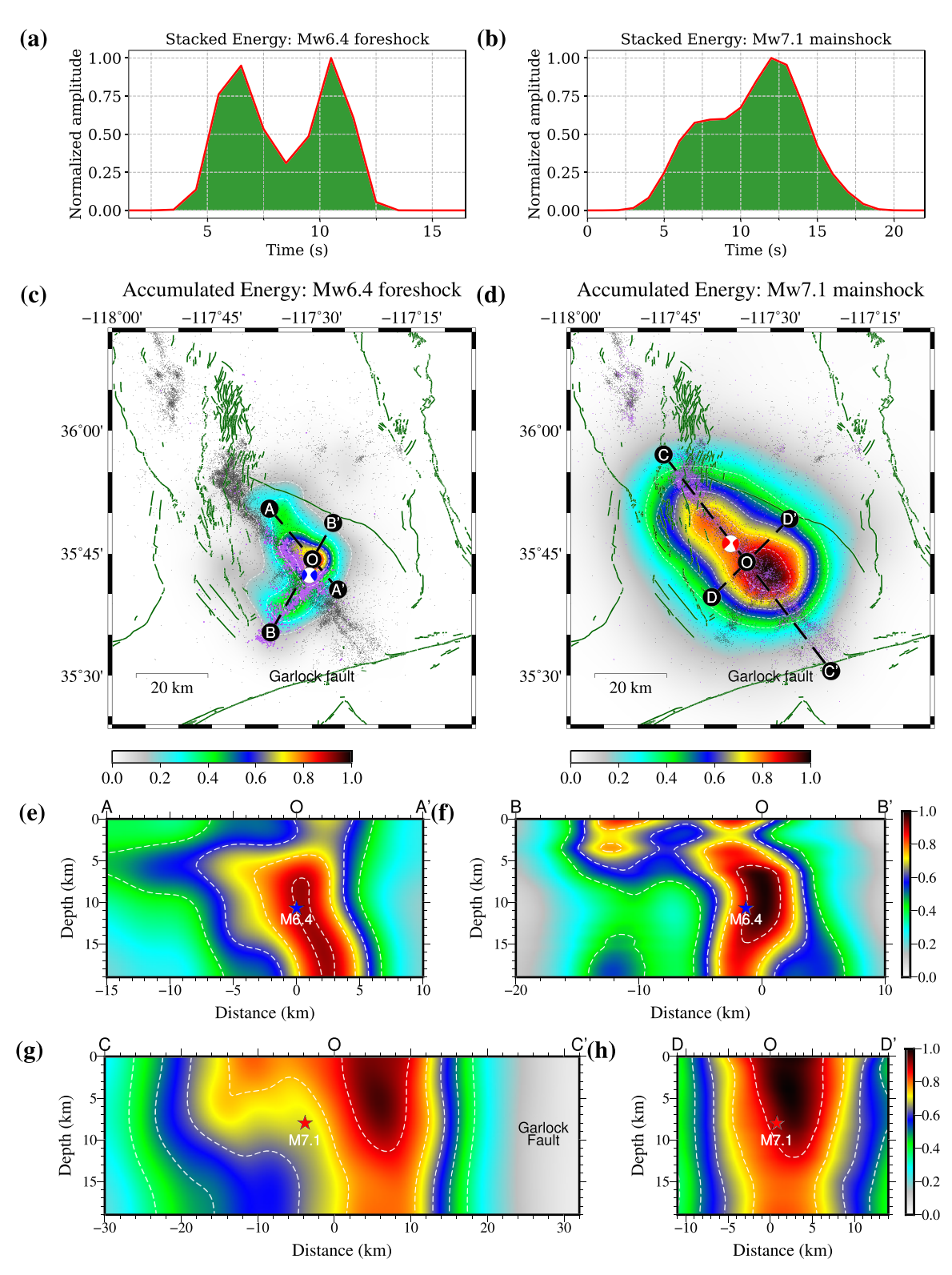


Figure 2. The time variations of the stacked radiation energy (a, b) and accumulated backprojection images (c–h). Panels (c) and (d) are the map view of the imaging results at hypocenter depths for the  $M_{\rm w}6.4$  foreshock and  $M_{\rm w}7.1$  mainshock, respectively. Panels (e)–(h) are the vertical profiles of the imaging results along the four dashed lines in panels (c) and (d). Black dots in panels (c) and (d) are the aftershocks within 27 days from 4 July 2019, collected from the SCEDC catalog. Purple dots in panel (c) are the aftershocks after the  $M_{\rm w}6.4$  foreshock, but before the  $M_{\rm w}7.1$  mainshock (about 34 hr). Purple dots in panel (d) are the aftershocks within four days after the  $M_{\rm w}7.1$  mainshock. Green solid lines are the mapped Quaternary faults from USGS. Blue and red stars in panels (e)–(h) denote the projections of CMT locations on these vertical profiles.

YANG ET AL. 5 of 11

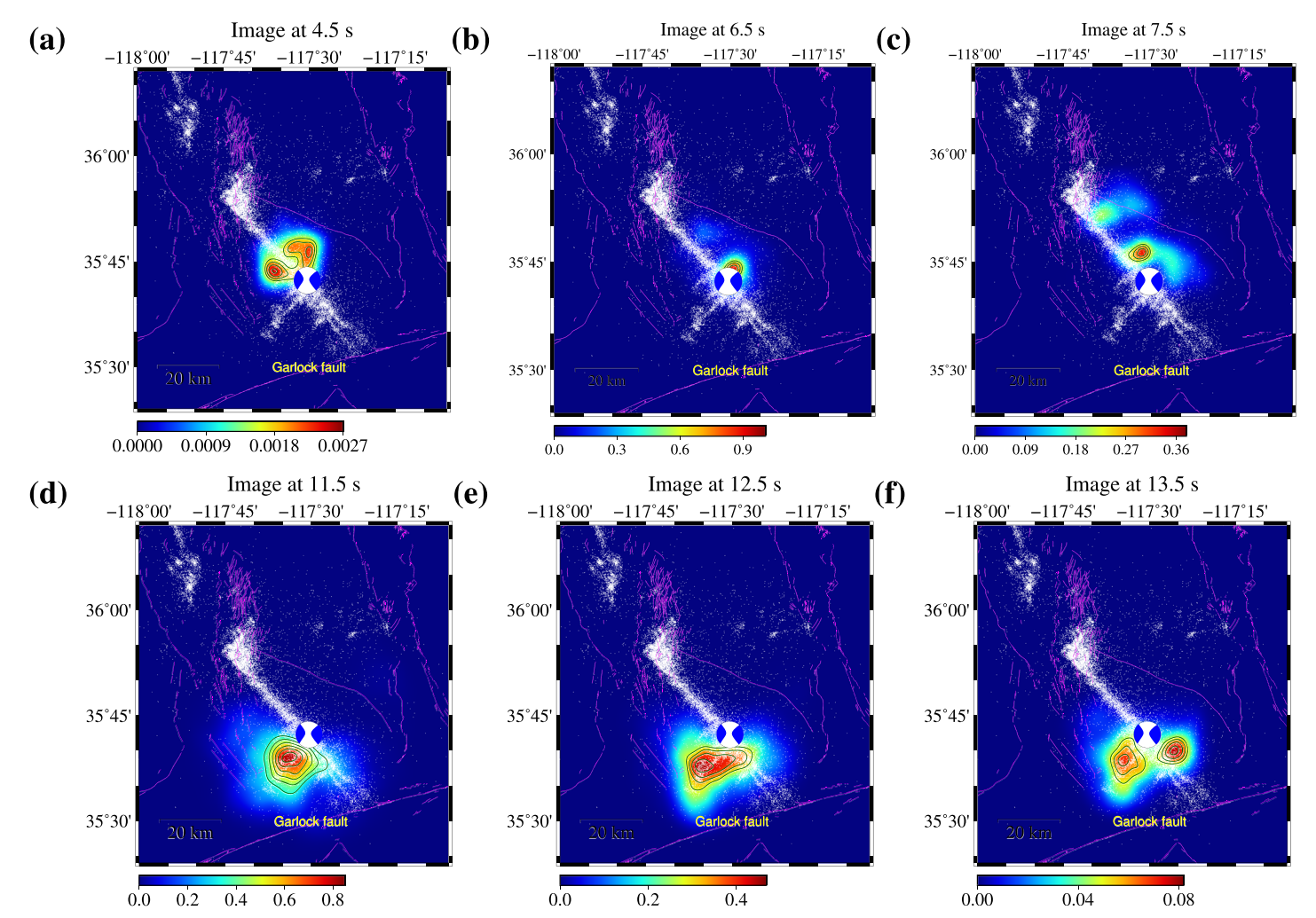


Figure 3. Time-lapse rupture propagation imaged using multiazimuth backprojection for the  $M_w$ 6.4 foreshock. White dots denote the aftershocks within 27 days from 4 July 2019, and purple solid lines are the mapped Quaternary faults (https://earthquake.usgs.gov/hazards/qfaults/). The blue beach ball denotes the CMT solution for the  $M_w$ 6.4 foreshock.

the hypothesis that the main fault plane can be represented using vertical fault segments (Liu et al., 2019; Ross et al., 2019).

The detailed rupture evolution of the  $M_{\rm w}$  6.4 foreshock is illustrated in Figure 3. Before producing large slips, the  $M_{\rm w}$  6.4 foreshock has a weak energy cluster on the backprojection image (Figure 3a), which is elongated along the NE-SW direction and spatially correlates with the orthogonal faults between the epicenters of the  $M_{\rm w}$ 6.4 foreshock and the  $M_{\rm w}$ 7.1 mainshock. This indicates that the small-scale NE-SW trending faults ruptured during the early stage of the  $M_w$ 6.4 event. Then, a large-amplitude cluster occurs near the  $M_w$ 6.4 epicenter (Figure 3b), indicating large slips within this region. Its location is consistent with the first subevent (E1) from Ross et al. (2019). Next, the energy cluster propagates to the northwest and travels about 8 km (Figure 3c), suggesting the  $M_{\rm m}$ 6.4 foreshock ruptured a NW-SE fault during t=5-8 s (the first energy peak in Figure 2a). Later, the rupture jumped to the large NE-SW trending fault (Figures 3d-3f). The peak amplitude on the backprojection images along the NE-SW fault segment occurred around t = 11.5 s (Figure 3d). The center of the energy cluster is located about 11 km southwest of the epicenter, which agrees with the third subevent (E3) location from Ross et al. (2019), as well as the large slip locations from Liu et al. (2019). After releasing the peak radiation energy, the rupture continued to propagate toward the southwest, and terminated about 20 km away from the epicenter (Figure 3e). The small-scale NE-SW trending faults within the southeast region of the epicenter appear to have ruptured after the long-distance faulting process (Figure 3f). Notably, there is a rupture gap about 3 s between the two energy peaks (Figure 2a). One explanation

YANG ET AL. 6 of 11

19448007, 2020, 9, Downloaded from https://agupubs.onlindibrary.wiley.com/doi/10.1029/2020GL087181 by University Of Texas - Dallas, Wiley Online Library on [16/02/2023]. See the Terms and Conditions (https://onlinelibrary.onli

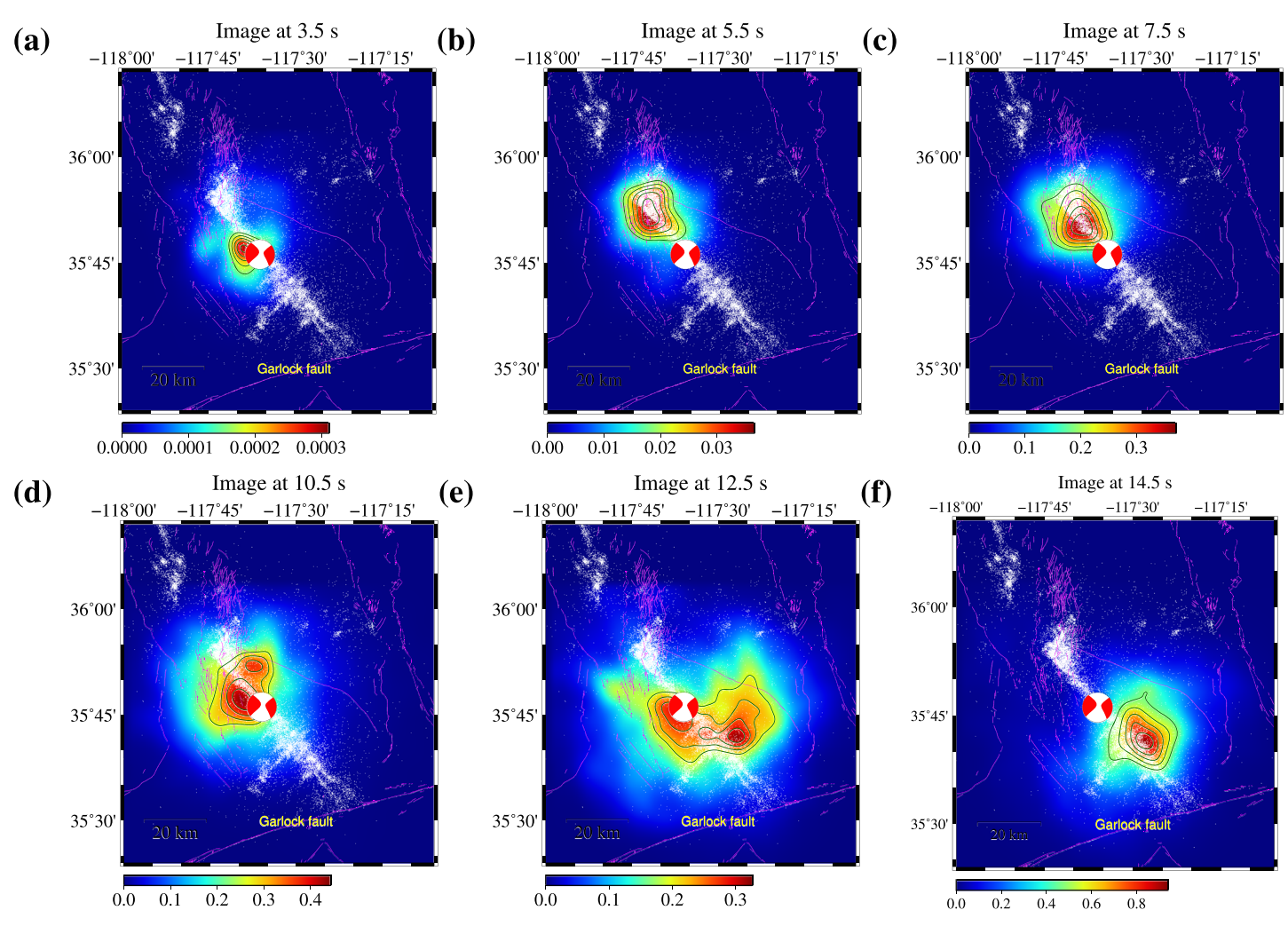


**Figure 4.** The same setting as Figure 3 except for the  $M_w$ 7.1 mainshock.

for this gap is that many small-scale faults slipped around the intersection, which cut across the main fault zone and provided the stress conditions for generating a large southwest striking rupture.

Furthermore, Figure 4 presents the rupture process of the  $M_w$ 7.1 mainshock. This event initialized near the hypocenter with small amplitudes (Figures 2b and 4a). In the following four seconds, the rupture propagated to the northwest and terminated upon arriving at the Coso volcanic field (Figures 4b and 4c). The spatial pattern of these energy clusters correlates well with the horsetail-like aftershock distributions within the Coso volcanic region. These results suggest the small-scale horsetail faults at the northwest terminus of the main fault zone slipped at the early stage of the  $M_w$ 7.1 mainshock. After that, the rupture turned to the southeast and released a large amount of energy close to the hypocenter around t = 10.5 s (Figures 2b and 4d), which correlates with the large slips from the finite-fault model presented by Liu et al. (2019). The occurrence of two local energy maxima in Figure 4d suggests a bilateral rupture process, which agrees with the E1 subsevent of the  $M_w$ 7.1 kinematic rupture model proposed by Ross et al. (2019). Subsequently, the rupture continued to propagate to the southeast (Figures 4e and 4f). Multiple local energy maxima on Figure 4e suggest complex bilateral slips between the  $M_w$ 7.1 epicenter and the intersection. In addition, the spatial pattern in Figure 4e indicates the NE-SW fault ruptured by the early  $M_{\rm m}$ 6.4 foreshock impeded the southern strand propagation of the bilateral rupture, leading to a slower speed than the northern strand. This cross fault impeding also results in large amplitudes along the northern strand within the bifurcation region, after the rupture passed through the intersection (Figure 4f). The large energy distribution along the northeastern strand agrees with Barnhart et al.'s (2019) observation that this strand has the majority of displacements within the southeast bifurcation region of the  $M_{w}$ 7.1 event.

YANG ET AL. 7 of 11

19448007, 2020, 9, Downloaded from https://agupubs.onlinelibrary.wiley.com/doi/10.1029/2020GL087181 by University Of Texas - Dallas, Wiley Online Library on [16/02/2023]. See the Terms and Conditions (https://onlinelibrary.wiley

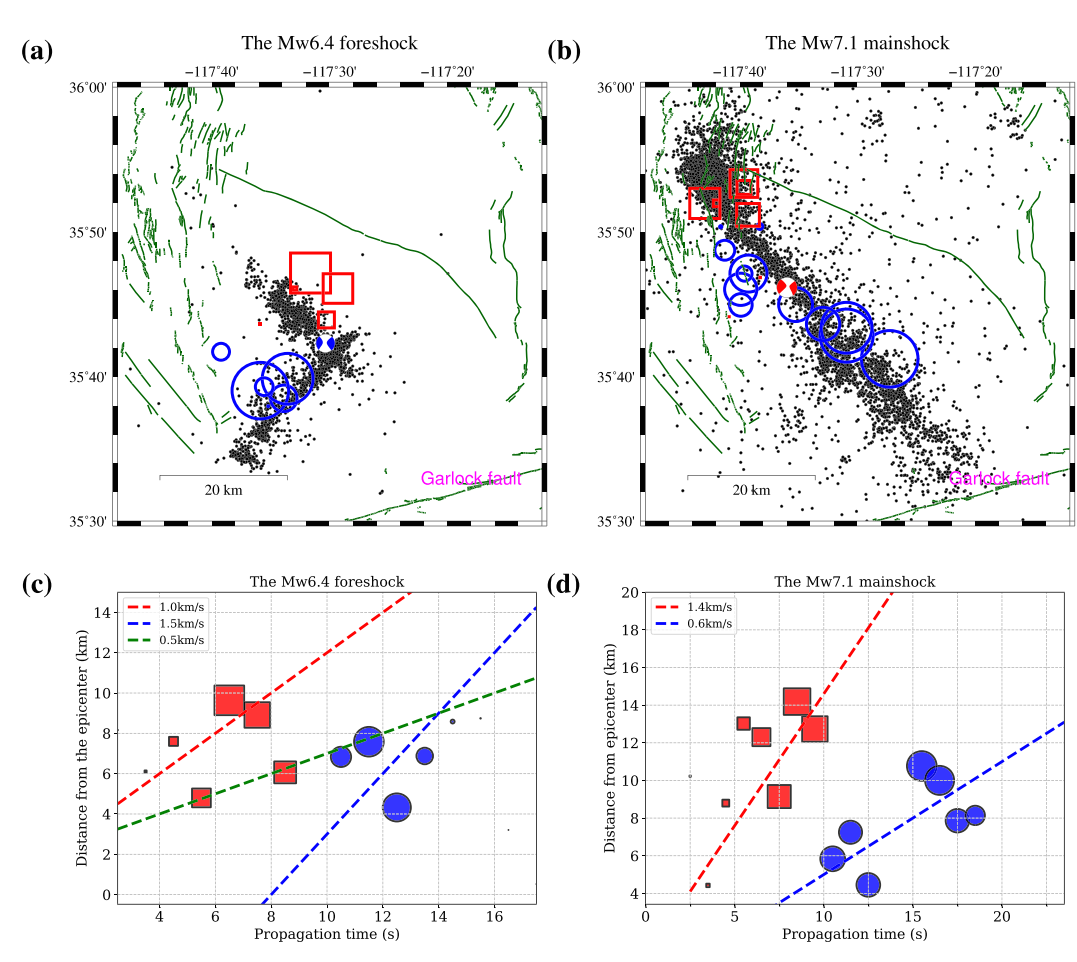


**Figure 5.** The map views of high-frequency maximum backprojection amplitudes (a, b), and diagrams of rupture propagation times versus distances (c, d) for the  $M_w$ 6.4 foreshock (left column) and  $M_w$ 7.1 mainshock (right column). Red squares and blue circles denote different rupture segments, and their sizes are proportional to image amplitudes. Red, blue and green lines indicate different rupture velocities. Black dots in panels (a) and (b) represent aftershocks.

# 5. Discussion

For the  $M_{\rm w}$ 6.4 foreshock, the "L-shape" pattern in the backprojection image spatially correlates well with the aftershock distributions (Figures 2c and 2e). The large image amplitudes (Figure S7) are also consistent with the large slip distributions in the finite-fault inversion model proposed by Liu et al. (2019). The time-lapse backprojection images in Figure 3 reveal that the two energy peaks in the time variations (Figure 2a) are associated with the rupture processes along different segments of the "L-shape" fault geometry. For example, the NW-SE trending fault ruptured at the early stage, with an average rupture velocity of 1.0 km/s (red squares and dashed line in Figures 5a and 5c). Subsequently, the NE-SW fault slipped with a faster rupture velocity around 1.5 km/s (blue circles and dashed line in Figures 5a and 5c). In addition, the slowest rupture velocity, about 0.5 km/s (green dashed line in Figure 5c), appears as a transition between the rupture processes along the NW-SE and NE-SW fault segments. Its propagation time corresponds to the energy gap between these two peaks in Figure 2a. This slow rupture process might be associated with small-scale slips that cut across the main NW-SE fault zone near the intersection.

The diagram of rupture propagation times versus epicentral distances for the  $M_w$ 7.1 mainshock is presented in Figures 5b and 5d, which shows different velocities at different segments. Along the northwesternmost segment, the  $M_w$ 7.1 mainshock shows a simple uniaxial rupture process (Figures 4a–4c), with a relatively fast propagation speed around 1.4 km/s (red squares and dashed line in Figures 5b and 5d). In contrast, the rupture propagation becomes slower (blue squares and dashed lines in Figures 5b and 5d), after it changes to the bilateral rupture mode. As shown in Figures 4e and 4f, the northern strand of the bilateral rupture

YANG ET AL. 8 of 11

has relatively larger energy than the southern strand. This difference might be related to the NE-SW cross fault ruptured by the  $M_w$ 6.4 foreshock. It slows down the rupture of the southern strand when the rupture front arrives at the intersection region. This phenomenon maybe similar to the stress shadowing observed in hydraulic fracturing (Nagel & Sanchez-Nagel, 2011; Yoon et al., 2015). When one fault slips, it decreases the stress within a region (shadow) near the fault plane, making it harder to rupture in the shadow region for subsequent events. The rupture velocities are slower than the local S wave speed (about 2.9 km/s at the depth of 5 km), which may be due to the immaturity of this fault system. In addition, the spatial pattern of the backprojection image for the  $M_w$ 7.1 event is consistent with slip distributions in Liu et al. (2019) (Figures S7 and S9).

Although the basic spatial patterns of the foreshock and mainshock ruptures presented in Figures 1-4 agree with finite-fault inversion results, their details are different at some locations. Possible reasons include the following aspects. First, the backprojection analysis is an adjoint-based imaging method, and its best spatial resolution is about one wavelength, which leads to smearing along horizontal and depth directions (Figures 2). In contrast, the finite-fault model is computed by solving a nonlinear inverse problem. Theoretically, it has a higher spatial resolution than backprojection results. But the backprojection does not need a priori information about the fault geometry and has a potential advantage of providing a posterior probability distribution for the rupture source mechanism process, rather than slip values at discrete locations only along predefined fault planes as in the finite-fault method. Second, data used in finite-fault inversions and backprojection analysis might be different. For example, Liu et al. (2019) use strong motion seismograms and GPS static displacements to invert for finite-fault parameters. We use all available regional seismic data around the epicenter. The sensitivities of these data might be different in terms of constraining coseismic ruptures. Third, high-frequency seismic radiation energy is commonly related to large contrasts of rupture properties or fault geometries. Therefore, the corresponding backprojection images reflect the margin of large slip patches and step over regions, which might be different from the true slip distributions (Kiser & Ishii 2011; Koper et al., 2012). Fourth, the complex near- and intermediate-field interferences might lead to nonconstructive interference on stacking results and reduce backprojection accuracy.

The rupture trajectories of the  $M_w$ 6.4 foreshock are distinct from the  $M_w$ 7.1 mainshock (Figures 1–4), indicating that the faults do not prefer to slip repeatedly during one earthquake sequence. These nonrepeatable rupturing characteristics for the  $M_w$ 6.4 foreshock and  $M_w$ 7.1 mainshock suggest the kinematic connections between these two events are not significantly strong. With high-resolution aftershock analysis, Ross et al. (2019) proposed that there is a 4-km barrier that impeded the immediate nucleation of the  $M_w$ 7.1 mainshock after the  $M_w$ 6.4 foreshock, and the mainshock is triggered until the barrier is reduced by a series of moderate-sized aftershocks. From calculations of the static Coulomb stress change imposed by the  $M_w$ 6.4 foreshock, Goldberg et al. (2019) and Barnhart et al. (2019) found a static stress change along the fault planes associated with the  $M_w$ 7.1 mainshock, and its hypocenter is located in a region with increased Coulomb stress. These studies demonstrate that the relation of these two events can be partially explained using dynamic stress analysis. The detailed physical mechanism for complex orthogonal faulting processes cannot be resolved by this study and still requires further investigations.

Furthermore, the radiation patterns of elastic source mechanism versus azimuths have stronger effects on regional seismograms than teleseismic data. In this study, we obtain constructive waveform stacking by choosing an appropriate number of azimuth clusters. An improved strategy might be to develop an optimal weighting factor according to the nodal plane information, which can be computed from centroid moment tensor solutions. These optimal azimuthal clusters and weights might help to further enhance imaging quality and spatial resolution, which needs further investigations.

### 6. Conclusions

In this study, we develop a multiazimuth backprojection imaging approach using regional seismic networks and apply it to the 2019 Ridgecrest earthquake sequence. The dense seismic arrays deployed in Southern California allow us to accurately image the time-lapse rupture processes of the  $M_w$ 6.4 foreshock and  $M_w$ 7.1 mainshock. The spatial patterns of the time-integrated backprojection images of these two events agree with the fault geometry determined by surface breaks and subsurface aftershock distributions. The  $M_w$ 6.4 foreshock has an "L-shape" rupture trajectory, which includes a short NW-SE segment and a long NE-SW

YANG ET AL. 9 of 11

1944807, 2020, 9, Downboated from https://agupubs.onlinelibrary.wiky.com/doi/10.102/92020GL087181 by University Of Texas - Dallas, Wiley Online Library on [16/02/2023]. See the Terms and Conditions (https://onlinelibrary.wiky.com/rems-and-conditions) on Wiley Online Library or rules of use; OA articles are governed by the applicable Ceravive Commons

Acknowledgments

Seismic waveforms were downloaded from the SCEDC (https://scedc. caltech.edu/eq-catalogs/index.html). The 3-D crustal velocity model for California was developed by Lin et al. (2010), which can be downloaded online (https://galin.weebly.com/ ca-statewide.html). The centroid moment tensor solutions are downloaded online (https://www. globalcmt.org/). Waveform data were processed using SAC (https://ds.iris. edu/files/sac-manual/), and OBSPY (https://github.com/obspy/obspy/). Imaging results are plotted using GMT (https://gmt.soest.hawaii.edu/projects/ gmt/). This research is supported by the PhD program at Department of Geosciences, the University of Texas at Dallas. We appreciate suggestions and comments from Editor Gavin Hayes and two anonymous reviewers, which significantly improved the manuscript. We are grateful to the Texas Advanced Computing Center for providing computational resources. This paper is a contribution number of 1363 from Department of Geosciences at the University of Texas at Dallas.

# ture processes for these two events. For instance, the $M_w$ 6.4 foreshock initialized near the hypocenter, then propagated to the northwest with a velocity around 1.0 km/s, and finally jumped to a long NE-SW trending fault with a rupture velocity around 1.5 km/s. The $M_w$ 7.1 mainshock initialized close to the hypocenter, then propagated to the northwest until reaching the Coso volcanic field, and later turned to the southeast and ruptured about 50 km with an average velocity of 0.6 km/s. Multiple local energy maxima on backprojection images indicate that the $M_w$ 7.1 mainshock involves a complex bilateral rupture process, with nonuniform rupture speeds along different fault segments. These results demonstrate that with dense regional arrays and 3-D crustal velocity models, backprojection analysis can be used to accurately characterize coseismic rupture propagations for large earthquakes.

NW-SE trending fault. The backprojection images at different propagation times illustrate the detailed rup-

# References

- Allen, R. M., & Kanamori, H. (2003). The potential for earthquake early warning in Southern California. Science, 300(5620), 786-789. https://doi.org/10.1126/science.1080912
- Atkinson, G. M. (1993). Earthquake source spectra in eastern North America. Bulletin of the Seismological Society of America, 83(6), 1778-1798. https://pubs.geoscienceworld.org/bssa/article-pdf/83/6/1778/270781%4/BSSA0830061778.pdf
- Atkinson, G. M., & Silva, W. (1997). An empirical study of earthquake source spectra for California earthquakes. Bulletin of the Seismological Society of America, 87(1), 97-113.
- Atzori, S., Hunstad, I., Chini, M., Salvi, S., Tolomei, C., Bignami, C., et al. (2009). Finite fault inversion of DInSAR coseismic displacement of the 2009 L'Aquila earthquake (central Italy). Geophysical Research Letters, 36, L15305. https://doi.org/10.1029/2009GL039293
- Barnhart, W. D., Hayes, G. P., & Gold, R. D. (2019). The July 2019 Ridgecrest, California earthquake sequence: Kinematics of slip and stressing in cross-fault ruptures. Geophysical Research Letters, 46, 11,859-11,867. https://doi.org/10.1029/2019GL084741
- Beresnev, I. A., & Atkinson, G. M. (2002). Source parameters of earthquakes in eastern and western North America based on finite-fault
- modeling. Bulletin of the Seismological Society of America, 92(2), 695-710. https://doi.org/10.1785/0120010101,. Brandenberg, S. J., Wang, P., Nweke, C. C., Hudson, K., Mazzoni, S., Bozorgnia, Y., et al. (2019). Preliminary report on engineering and
- geological effects of the July 2019 Ridgecrest earthquake sequence: Geotechnical Extreme Event Reconnaissance Association. Chen, K., Avouac, J.-P., Aati, S., Milliner, C., Zheng, F., & Shi, C. (2020). Cascading and pulse-like ruptures during the 2019 Ridgecrest
- earthquakes in the Eastern California Shear Zone. Nature Communications, 11(1), 1-8.
- Crowell, B. W., Bock, Y., & Melgar, D. (2012). Real-time inversion of GPS data for finite fault modeling and rapid hazard assessment. Geophysical Research Letters, 39, L09305. https://doi.org/10.1029/2012GL051318
- Crowell, B. W., Bock, Y., & Squibb, M. B. (2009). Demonstration of earthquake early warning using total displacement waveforms from real-time GPS networks. Seismological Research Letters, 80(5), 772-782.
- D'Amico, S., Koper, K. D., Herrmann, R. B., Akinci, A., & Malagnini, L. (2010). Imaging the rupture of the Mw 6.3 April 6, 2009 L'Aquila, Italy earthquake using back-projection of teleseismic P-waves. Geophysical Research Letters, 37, L03301. https://doi.org/10. 1029/2009GL042156
- Dettmer, J., Benavente, R., Cummins, P. R., & Sambridge, M. (2014). Trans-dimensional finite-fault inversion. Geophysical Journal International, 199(2), 735-751. https://doi.org/10.1093/gji/ggu280
- Dziewonski, A. M., Chou, T.-A., & Woodhouse, J. H. (1981). Determination of earthquake source parameters from waveform data for studies of global and regional seismicity. Journal of Geophysical Research, 86, 2825-2852. https://doi.org/10.1029/JB086iB04p02825
- Dziewonski, A. M., & Woodhouse, J. H. (1983). An experiment in systematic study of global seismicity: Centroid-moment tensor solutions for 201 moderate and large earthquakes of 1981. Journal of Geophysical Research, 88, 3247-3271. https://doi.org/10.1029/
- Falck, C., Ramatschi, M., Subarya, C., Bartsch, M., Merx, A., Hoeberechts, J., & Schmidt, G. (2010). Near real-time GPS applications for tsunami early warning systems. Natural Hazards and Earth System Sciences, 10(2), 181-189.
- Fomel, S. (1997). A variational formulation of the fast marching Eikonal solver. SEP-95: Stanford Exploration Project.
- Goldberg, D. E., Melgar, D., Thomas, A. M., Sahakian, V. J., Xu, X., Geng, J., & Crowell, B. W. (2019). Complex rupture of an immature fault zone: A simultaneous kinematic model of the 2019 Ridgecrest, CA earthquakes.
- Hartzell, S. H. (1978). Earthquake aftershocks as Green's functions. Geophysical Research Letters, 5(1), 1-4. https://doi.org/10.1029/ GL005i001p00001
- Hayes, G. P. (2011). Rapid source characterization of the 2011 Mw9.0 off the Pacific coast of Tohoku earthquake. Earth, Planets and Space, 63(7), 4.
- Hayes, G. P., Rivera, L., & Kanamori, H. (2009). Source inversion of the W-phase: Real-time implementation and extension to low magnitudes. Seismological Research Letters, 80, 817-822. https://doi.org/10.1785/gssrl.80.5.817
- Ishii, M., Shearer, P. M., Houston, H., & Vidale, J. E. (2005). Extent, duration and speed of the 2004 Sumatra-Andaman earthquake imaged by the Hi-Net array. Nature, 435(7044), 933.
- Ji, C., Helmberger, D. V., Alex Song, T.-R., Ma, K.-F., & Wald, D. J. (2001). Slip distribution and tectonic implication of the 1999 Chi-Chi, Taiwan, earthquake. Geophysical Research Letters, 28(23), 4379-4382. https://doi.org/10.1029/2001GL013225
- Ji, C., Wald, D. J., & Helmberger, D. V. (2002). Source description of the 1999 Hector Mine, California, earthquake, Part I: Wavelet domain inversion theory and resolution analysis. Bulletin of the Seismological Society of America, 92(4), 1192-1207.
- Johnson, K. M., Hsu, Y.-J., Segall, P., & Yu, S.-B. (2001). Fault geometry and slip distribution of the 1999 Chi-Chi, Taiwan earthquake imaged from inversion of GPS data. Geophysical Research Letters, 28(11), 2285-2288. https://doi.org/10.1029/2000GL012761
- Johnson, K. M., & Segall, P. (2004). Imaging the ramp-décollement geometry of the Chelungpu fault using coseismic GPS displacements from the 1999 Chi-Chi, Taiwan earthquake. Tectonophysics, 378(1), 123-139.
- Kiser, E., & Ishii, M. (2011). The 2010 Mw 8.8 Chile earthquake: Triggering on multiple segments and frequency-dependent rupture behavior. Geophysical Research Letters, 38(7).
- Kiser, E., & Ishii, M. (2017). Back-projection imaging of earthquakes. Annual Review of Earth and Planetary Sciences, 45, 271–299.

YANG ET AL. 10 of 11

- Kiser, E., Ishii, M., Langmuir, C. H., Shearer, P., & Hirose, H. (2011). Insights into the mechanism of intermediate-depth earthquakes from source properties as imaged by back projection of multiple seismic phases. *Journal of Geophysical Research*, 116, B06310. https://doi.org/10.1029/2010JB007831
- Koper, K. D., Hutko, A. R., Lay, T., & Sufri, O. (2012). Imaging short-period seismic radiation from the 27 February 2010 Chile (Mw 8.8) earthquake by back-projection of P, PP, and PKIKP waves. *Journal of Geophysical Research*, 117, B02308. https://doi.org/10.1029/2011JB008576
- Lin, G., Thurber, C. H., Zhang, H., Hauksson, E., Shearer, P. M., Waldhauser, F., et al. (2010). A California statewide three-dimensional seismic velocity model from both absolute and differential times. *Bulletin of the Seismological Society of America*, 100(1), 225–240.
- Liu, P., & Archuleta, R. J. (2004). A new nonlinear finite fault inversion with three-dimensional Green's functions: Application to the 1989 Loma Prieta, California, earthquake. *Journal of Geophysical Research*, 109, B02318. https://doi.org/10.1029/2003JB002625
- Liu, C., Lay, T., Brodsky, E. E., Dascher-Cousineau, K., & Xiong, X. (2019). Coseismic rupture process of the large 2019 Ridgecrest earth-quakes from joint inversion of geodetic and seismological observations. *Geophysical Research Letters*, 46, 11,820–11,829. https://doi.org/10.1029/2019GL084949
- Liu, Q., Polet, J., Komatitsch, D., & Tromp, J. (2004). Spectral-element moment tensor inversions for earthquakes in Southern California. Bulletin of the Seismological Society of America, 94(5), 1748–1761. https://doi.org/10.1785/012004038
- Liu, Z., Song, C., Meng, L., Ge, Z., Huang, Q., & Wu, Q. (2017). Utilizing a 3D global *P*-wave tomography model to improve backprojection imaging: A case study of the 2015 Nepal earthquake. *Bulletin of the Seismological Society of America*, 107(5), 2459–2466.
- Melgar, D., Bock, Y., & Crowell, B. W. (2012). Real-time centroid moment tensor determination for large earthquakes from local and regional displacement records. Geophysical Journal International, 188(2), 703–718.
- Meng, L., Zhang, A., & Yagi, Y. (2016). Improving back projection imaging with a novel physics-based aftershock calibration approach: A case study of the 2015 Gorkha earthquake. Geophysical Research Letters, 43(2), 628-636. https://doi.org/10.1002/2015GL067034
- Minson, S. E., Murray, J. R., Langbein, J. O., & Gomberg, J. S. (2014). Real-time inversions for finite fault slip models and rupture geometry based on high-rate GPS data. *Journal of Geophysical Research: Solid Earth*, 119, 3201–3231. https://doi.org/10.1002/2013JB010622
- Nagel, N. B., & Sanchez-Nagel, M. (2011). Stress shadowing and microseismic events: A numerical evaluation. In SPE Annual Technical Conference and Exhibition (pp. 1–14). Society of Petroleum Engineers.
- Nakata, N., & Beroza, G. C. (2016). Reverse time migration for microseismic sources using the geometric mean as an imaging condition. Geophysics, 81(2), KS51–KS60.
- Ross, Z. E., Idini, B., Jia, Z., Stephenson, O. L., Zhong, M., Wang, X., et al. (2019). Hierarchical interlocked orthogonal faulting in the 2019 Ridgecrest earthquake sequence. *Science*, 366(6463), 346–351.
- Satriano, C., Lomax, A., & Zollo, A. (2008). Real-time evolutionary earthquake location for seismic early warning. Bulletin of the Seismological Society of America, 98(3), 1482–1494. https://doi.org/10.1785/0120060159
- Tinti, E., Scognamiglio, L., Michelini, A., & Cocco, M. (2016). Slip heterogeneity and directivity of the ML 6.0, 2016, Amatrice earthquake estimated with rapid finite-fault inversion. *Geophysical Research Letters*, 43(20), 10–745. https://doi.org/10.1002/2016GL071263
- Wald, D. J., & Heaton, T. H. (1994). Spatial and temporal distribution of slip for the 1992 Landers, California, earthquake. *Bulletin of the Seismological Society of America*, 84(3), 668–691. https://pubs.geoscienceworld.org/bssa/article-pdf/84/3/668/2708060%/BSSA0840030668.
- Walker, K. T., & Shearer, P. M. (2009). Illuminating the near-sonic rupture velocities of the intracontinental Kokoxili Mw 7.8 and Denali fault Mw 7.9 strike-slip earthquakes with global P wave back projection imaging. *Journal of Geophysical Research*, 114, B02304. https://doi.org/10.1029/2008JB005738
- Wang, D., & Mori, J. (2011). Rupture process of the 2011 off the Pacific coast of Tohoku earthquake (Mw9.0) as imaged with back-projection of teleseismic *P*-waves. *Earth, planets and space*, 63(7), 17.
- Xu, Y., Koper, K. D., Sufri, O., Zhu, L., & Hutko, A. R. (2009). Rupture imaging of the Mw 7.9 12 May 2008 Wenchuan earthquake from back projection of teleseismic *P* waves. *Geochemistry, Geophysics, Geosystems, 10*, Q04006. https://doi.org/10.1029/2008GC002335
- Yoon, J. S., Zimmermann, G., & Zang, A. (2015). Numerical investigation on stress shadowing in fluid injection-induced fracture propagation in naturally fractured geothermal reservoirs. *Rock Mechanics and Rock Engineering*, 48(4), 1439–1454.
- Yue, H., Lay, T., Rivera, L., An, C., Vigny, C., Tong, X., & Báez Soto, J. C. (2014). Localized fault slip to the trench in the 2010 Maule, Chile Mw8.8 = earthquake from joint inversion of high-rate GPS, teleseismic body waves, InSAR, campaign GPS, and tsunami observations. Journal of Geophysical Research: Solid Earth, 119, 7786–7804. https://doi.org/10.1002/2014JB011340

YANG ET AL. 11 of 11